Comparison of COSMIC ionospheric measurements with ground-based observations and model predictions: Preliminary results

Jiuhou Lei,[1] Stig Syndergaard,[2] Alan G. Burns,[1] Stanley C. Solomon,[1] Wenbin Wang,[1] Zhen Zeng,[1,2] Raymond G. Roble,[1] Qian Wu,[1] Ying-Hwa Kuo,[2] John M. Holt,[3] Shun-Rong Zhang,[3] David L. Hysell,[4] Fabiano S. Rodrigues,[4] and Chien H. Lin[5]

[1] Electron densities retrieved from the Constellation Observing System for Meteorology, Ionosphere, and Climate (COSMIC) radio occultation (RO) measurements are compared with those measured by incoherent scatter radars (ISR) and ionosondes in this paper. These results show that electron density profiles retrieved from COSMIC RO data are in agreement with the ISR and ionosonde measurements. The ionospheric characteristics (N_mF_2 and h_mF_2) derived from the COSMIC satellites are also compared with those calculated by the latest International Reference Ionosphere model (IRI-2001) and the National Center for Atmospheric Research Thermosphere-Ionosphere-Electrodynamics General Circulation Model (NCAR-TIEGCM). The comparison of the magnitude of the COSMIC N_mF_2 data with those calculated by the IRI model and the TIEGCM is good. However, features such as the north-south asymmetry and longitudinal variation of the equatorial anomaly that are seen in the COSMIC data and the TIEGCM simulations are not fully present in the IRI model. On the other hand, the TIEGCM produces a stronger winter anomaly than that seen in either the COSMIC data or the IRI model.

1. Introduction

[2] A constellation of six satellites, called the Constellation Observing System for Meteorology, Ionosphere, and Climate (COSMIC or FORMOSAT-3), was launched on 15 April 2006 from Vandenberg Air Force Base, California [*Schreiner et al.*, 2007]. Three different instruments make up the science payload of the COSMIC satellites. The instrument that interests us here is the advanced GPS receiver developed by the Jet Propulsion Laboratory. It is used to obtain atmospheric and ionospheric measurements through phase and Doppler shifts of radio signals. The Doppler shift of the GPS L-band signals received by a low Earth orbit (LEO) satellite is used to compute the amount of signal bending that occurs as the GPS satellite sets or rises through the Earth's atmosphere as seen from LEO [e.g., *Rocken et al.*, 2000]. The bending angles are related to the vertical gradients of atmospheric and ionospheric refractivity. The refractivity is directly proportional to ionospheric electron density above 80 km altitude. Through the assumption of spherical symmetry, electron density profiles can be retrieved from either the bending angles or the total electron content data (computed from the L1 and L2 phase difference) obtained from the GPS occultations [e.g., *Hajj and Romans*, 1998; *Schreiner et al.*, 1999].

[3] The satellites were launched from the same rocket and initially followed the same orbit, with all six moving along the same path at 512 km. The satellites are currently being sequentially raised to orbits at around 800 km. The time delay for this increase in altitude is designed to spread the orbital planes, so the individual satellites are 30 degrees apart. The data used in this study primarily reflect the original configuration of the six satellites, when they were traveling in almost the same orbit, sequentially sampling at the same local time. The longitudes of the observations changed with changing universal time. Later studies will be able to make use of the final configuration of the satellites. At that time the COSMIC satellites will provide approximately 24 hours of local time coverage globally and will provide about 2500 vertical electron density profiles per day. When they achieve this distribution, the global ionospheric measurements by the COSMIC satellites will pro-

[1]High Altitude Observatory, National Center for Atmospheric Research, Boulder, Colorado, USA.

[2]COSMIC Project Office, University Corporation for Atmospheric Research, Boulder, Colorado, USA.

[3]Haystack Observatory, Massachusetts Institute of Technology, Westford, Massachusetts, USA.

[4]Department of Earth and Atmospheric Science, Cornell University, Ithaca, New York, USA.

[5]National Space Organization, Hsinchu, Taiwan.

vide a great opportunity to investigate global ionospheric structures and their variations.

[4] The objective of the present paper is to assess the early ionospheric results from the COSMIC satellites by comparing electron densities retrieved from COSMIC radio occultation (RO) measurements with those observed by Millstone Hill (42.6N, 71.5W) and Jicamarca (11.9S, 76.0W) incoherent scatter radars (ISR) and ionosondes at 31 stations. Comparisons are also made between these observations and electron densities calculated by the latest International Reference Ionosphere model (IRI-2001) [*Bilitza*, 2001] and the National Center for Atmospheric Research Thermosphere-Ionosphere-Electrodynamics General Circulation Model (NCAR-TIEGCM) [*Richmond et al.*, 1992].

2. COSMIC Measurements

[5] Each COSMIC satellite is equipped with four antennas, two of which are used for ionospheric electron density measurements (one for rising and one for setting occultations). These two antennas collect the L1 and L2 GPS phase data from up to 13 GPS satellites every second. The inversion of COSMIC data into electron density profiles is based on the difference between the L1 and L2 GPS phase path measurements.

[6] Under the assumption of straight-line propagation of GPS signals in the ionosphere, the difference between the L1 and L2 phase path measurements (except for a constant offset) is approximately proportional to the total electron content (TEC) along the line from the LEO satellite to the GPS satellite [e.g., *Syndergaard*, 2002]:

$$T - T_0 \approx \frac{f_1^2 f_2^2 (L_1 - L_2)}{C(f_1^2 - f_2^2)}. \tag{1}$$

In equation (1), T denotes the TEC, f_1 and f_2 are the two GPS carrier frequencies, L_1 and L_2 symbolizes the corresponding phase paths (measured in units of length), and C = 40.3082 m^3 s^{-2} is a constant. Since L_1 and L_2 are only measured up to a constant offset for each occultation, the derived TEC basically differ from the actual TEC by an arbitrary constant, T_0. However, the derived TEC is calibrated such that it approximately represents the portion of TEC below the LEO. This is done by subtracting the measurements at positive elevation angles from those at negative elevation angles as described in more detail by *Schreiner et al.* [1999]. Under the assumptions of spherical symmetry (i.e., assuming only vertical electron density gradients) and straight-line propagation, the calibrated TEC, $\tilde{T}$, is related to electron density, N, as a function of the radius from the Earth's center, r, as

$$\tilde{T}(p) = 2 \int_p^{p_{top}} \frac{rN(r)}{\sqrt{r^2 - p^2}} dr. \tag{2}$$

Here p is the distance from the Earth's center to the tangent point of a given straight line and $p_{top} \equiv r_{LEO}$ is the radius of the LEO. *Schreiner et al.* [1999] inverted equation (2) to obtain an expression for $N(r)$ given by

$$N(r) = -\frac{1}{\pi} \int_r^{r_{LEO}} \frac{d\tilde{T}/dp}{\sqrt{p^2 - r^2}} dp. \tag{3}$$

However, it can be shown (see below) that $d\tilde{T}/dp \rightarrow -\infty$ for $p \rightarrow p_{top}$. This would cause a numerical problem if we were to integrate equation (3) numerically, in particular for the upper part of the profile where r gets close to r_{LEO} and $p^2 - r^2$ is small while $d\tilde{T}/dp$ becomes large. The singularity at the lower limit, where $p^2 - r^2 \rightarrow 0$, could be eliminated by a change of variable. However, we did not go to great lengths to find a substitution scheme that would eliminate both the upper and the lower limit singularities. Instead we split the right-hand side of equation (2) into a sum of m integrals for a given $p = p_i$. Let $p_{i+k} = r_{i+k}$, $k = 0$, 1, …, m, denote the radius of $m + 1$ levels from p_i to $p_{i+m} = p_{top}$. We can then write equation (2) as

$$\tilde{T}(p_i) = \sum_{k=1}^m 2 \int_{p_{i+k-1}}^{p_{i+k}} \frac{rN(r)dr}{\sqrt{r^2 - p_i^2}}. \tag{4}$$

Assuming that $N(r)$ varies linearly with radius in between each level, the integrals in equation (4) can be solved analytically and $\tilde{T}(p_i)$ can be written in terms of $N(p_{i+k})$, $k = 0, 1, …, m$. The result is given in Appendix A. Equation (A2) is readily rearranged to yield $N(p_i)$ in terms of $\tilde{T}(p_i)$ and $N(p_{i+k})$ at the m levels above p_i:

$$N(p_i) = c_{i,0}^{-1} \left(\frac{\tilde{T}(p_i)}{p_i} - \sum_{k=1}^m c_{i,k} N(p_{i+k}) \right). \tag{5}$$

The dimensionless coefficients $c_{i,k}$, $k = 0, 1, …, m$, are given in Appendix A. Thus we can calculate the electron density profile recursively starting from the top if we know $N(p_{top})$. A first-order estimate of $N(p_{top})$ can be obtained by assuming $N(r) = N(r_{LEO}) \equiv N(p_{top})$ to be a constant for values of r near r_{LEO}. Under this condition, the integral in equation (2) can be solved to give

$$\tilde{T}(p) \approx 2N(p_{top}) \sqrt{2p_{top}(p_{top} - p)}. \tag{6}$$

Equation (6) indicates that $\tilde{T}(p)$ approximately behaves like a square root function for $p \approx p_{top}$ and that $d\tilde{T}/dp \rightarrow -\infty$ for $p \rightarrow p_{top}$, as mentioned above. This result seems to be valid in most practical cases when $N(r)$ is well behaved near the top. In practice, $N(r_{LEO})$ is derived from the occultation data by linear regression of the square of the calibrated TEC as a function of p (interpolated to the levels denoted by p_i) for the uppermost few kilometers. Having $N(r_{LEO})$, equation (5) is applied for $m = n - i = 1, 2, …, n - 1$, where n is the total number of levels in the profile ($n = 300$).

[7] The above description outlines the approach currently used for the inversion of the COSMIC ionospheric GPS occultation data at the University Corporation for Atmospheric Research (UCAR) COSMIC Data Analysis and Archival Center (CDAAC). Several assumptions and approximations are made: (1) proportionality between re-
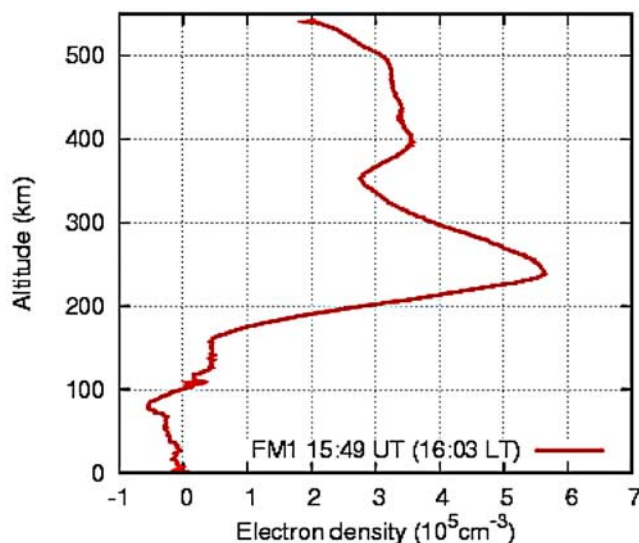
Figure 1. Example of retrieved electron density profile from COSMIC FM1 on 9 August 2006 (COSMIC Data Analysis and Archival Center ID: C001.2006.221.15. 50.G22), seemingly severely affected above 350 km by the presence of horizontal gradients (see Figure 2). The UT and LT times correspond to when the location of the tangential point is at the F_2 peak height (near 230 km).

trajectory indicates the point in the retrieved profile where there is an apparent local minimum at about 350 km. Most likely, the enhanced electron density above 350 km in Figure 1 is induced by the horizontal gradients, the vertical TEC being much larger to the north than to the south of the white dot in Figure 2. Below 100 km the retrieved electron density in Figure 1 becomes slightly negative, which is presumably also a result of the horizontal gradients and the assumption of spherical symmetry in the retrieval. Several studies have attempted to mitigate the errors induced by horizontal gradients using different approaches [e.g., *Hajj and Romans*, 1998; *Schreiner et al.*, 1999; *Hernandez-Pajares et al.*, 2000; *Garcia-Fernandez et al.*, 2003; *Tsai and Tsai*, 2004], but any such approach has yet to be applied routinely to the COSMIC data.

[9] Besides the retrieval errors discussed above, a small fraction of the COSMIC electron density profiles are affected by cycle slips in the GPS phase data. In some cases this results in obviously distorted profiles, whereas in other cases the errors due to cycle slips are more subtle.

3. Results

[10] Inverted electron density profiles from the COSMIC measurements during days 152–265, 2006, provided by CDAAC, are compared with ground based data and model

fractivity and electron density, (2) straight-line signal propagation, (3) spherical symmetry of electron density, (4) circular satellite orbits, and (5) first-order estimate of the electron density at the top. However, the assumption of spherical symmetry is by far the most significant source of error in the retrieval of the electron density profiles (when interpreted as actual vertical profiles). The errors that are induced because of this assumption probably overshadow the errors due to all other approximations in all cases. Previous works indicate that in cases of large N_mF_2 values, this assumption can result in either positive or negative errors larger than 10^5 cm^{-3} at altitudes below ~150 km [e.g., *Garcia-Fernandez et al.*, 2003; *Syndergaard et al.*, 2006]. Since equation (2) is already based on the assumption of spherical symmetry, this assumption also introduces an error in the first-order estimate of the electron density at the top.
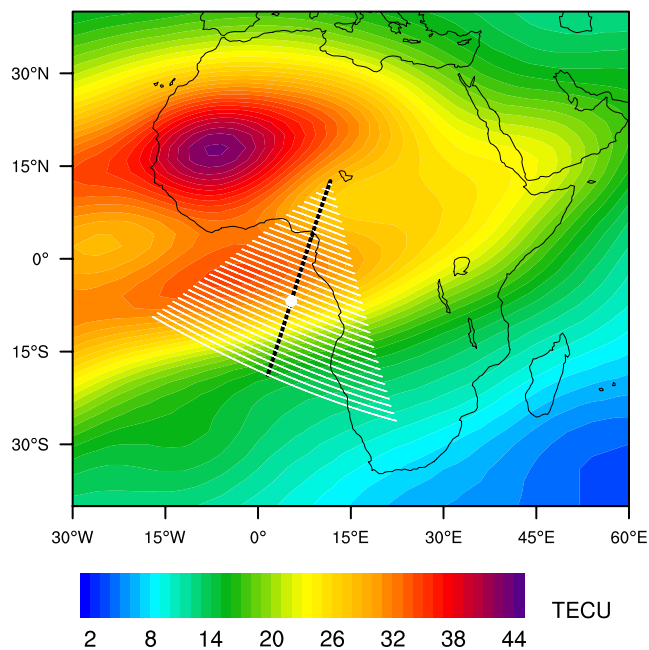
[8] As an example of the possible influence of horizontal gradients on the retrievals, Figure 1 shows a retrieved profile from one of the COSMIC satellites, which on 9 August 2006 observed a GPS RO across the southern part of the afternoon equatorial anomaly. The geometry of the occultation measurement on a map is shown in Figure 2. Figure 2 also shows the vertical TEC in the area (close to the time of observation) obtained from the Jet Propulsion Laboratory Global Ionospheric Maps. The black line across the map indicates the location of the tangent points during this setting occultation, starting on the African continent at about 540 km altitude and ending in the South Atlantic at about 100 km altitude. The white lines going across the tangent point trajectory are the portions of the GPS-LEO links that are below the LEO altitude. As the GPS satellite sets, the portion of the links below the orbit altitude becomes longer. The single white dot on the tangent point

Figure 2. The geometry for the retrieval of the electron density profile shown in Figure 1 superimposed on a map of the vertical total electron content (TEC) obtained from the Jet Propulsion Laboratory Global Ionospheric Maps (9 August 2006, 1530 UT). The COSMIC satellite moves southward across the African continent while receiving signals from a setting GPS satellite at an angle toward the west. The black line indicates the tangent point trajectory, and the white lines indicate the portions of the GPS-low Earth orbit (LEO) links that are below the LEO altitude. The white dot corresponds to when the tangential point is at the local electron density minimum near 350 km in Figure 1.
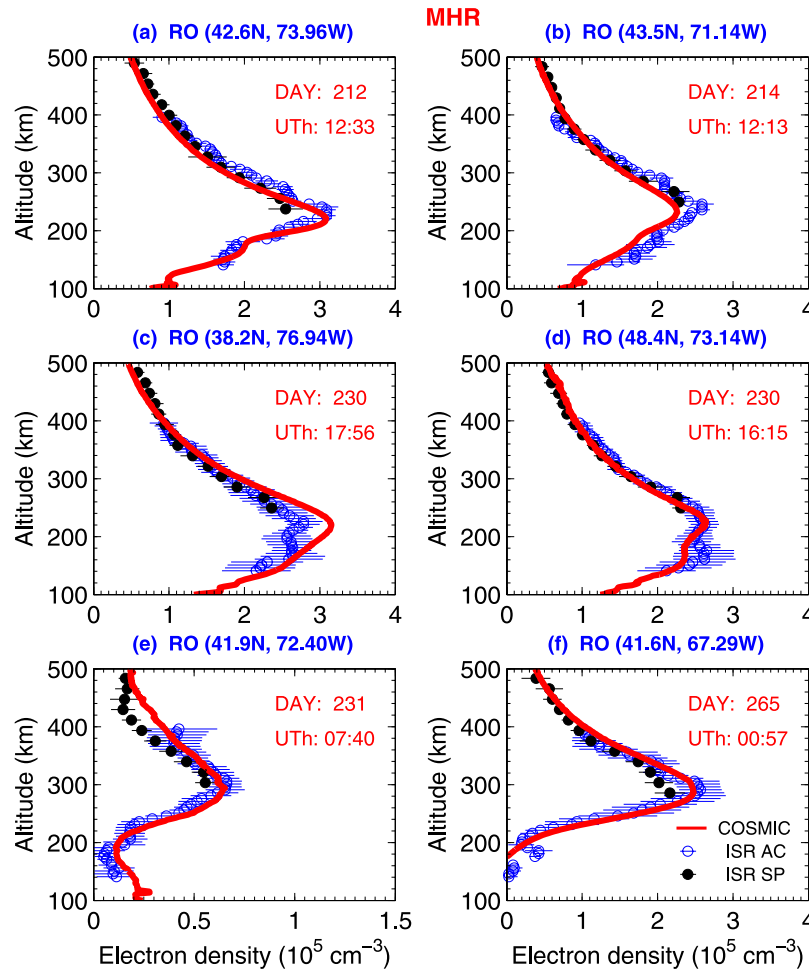
Figure 3. (a–f) Comparison of the COSMIC electron density profiles (solid lines) near Millstone Hill (42.6°N, 71.5°W) with those measured by Millstone Hill incoherent scatter radars (ISR) at the same time. ISR AC stands for alternate code data, and ISR SP stands for single-pulse data. The latitude and longitude of the radio occultation (RO) electron density profile at the F_2 peak height are shown at the top of each panel.

predictions in this study. The location of the tangential point at the F_2 peak height h_mF_2 is defined as the site of an occultation event [*Jakowski et al.*, 2002]. A least-squares fitting of the RO electron density profile at the F_2 layer to a two-layer Chapman function [*Lei et al.*, 2004, 2005] is performed:
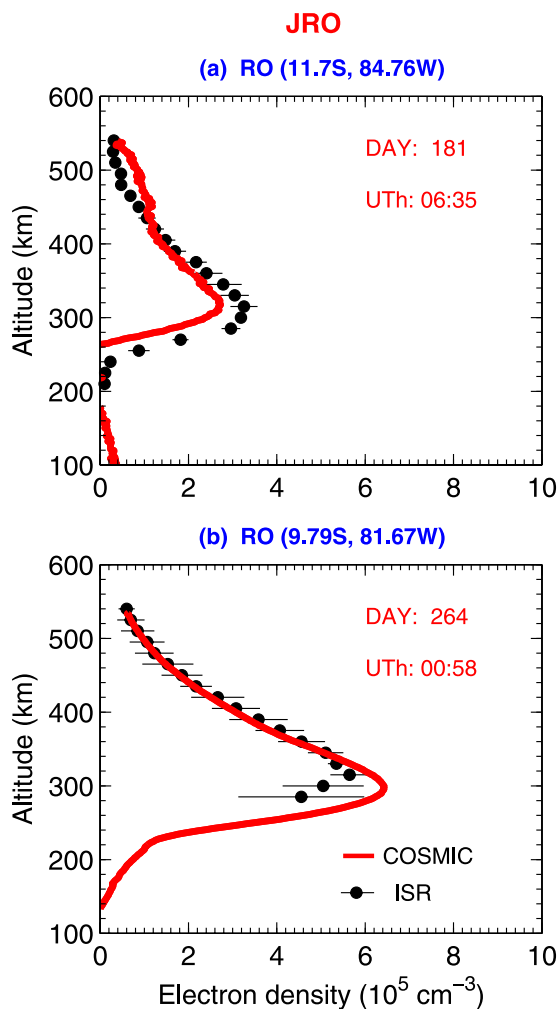
$$N(h) = N_mF_2 \exp[0.5(1 - z - e^{-z})], \qquad z = (h - h_mF_2)/H(h). \tag{7}$$

We take the Chapman scale height to be $H(h) = A_1(h - h_mF_2) + H_m$ in the bottomside and $H(h) = A_2(h - h_mF_2) + H_m$ in the topside. Here, N_mF_2, h_mF_2, H_m, A_1, and A_2 are adjustable parameters, and can be determined by using the least-squares fitting approach. This brings in the best match with the RO electron density profiles $N(h)$ at F_2 region [see *Lei et al.*, 2005]. Then seriously distorted electron density profiles with abnormal scale height at peak height ($H_m < 20$ km or $H_m > 100$ km), as well as those with the correlation coefficient (between the fitted and observed profiles) of determination less than 0.9, are discarded in the following analysis to insure the integrity of the results. About 9% of the COSMIC electron density profiles were discarded after applying the rejection criteria.

3.1. Comparison With ISR and Ionosonde Observations

[11] ISRs provide very good data to validate the COSMIC retrieved electron densities because they can probe not only the ionospheric characteristics but also the whole electron density profile. Carefully calibrated ISR electron density data on 31 July, 2 August, 18–19 August, and 20–22 September 2006 at Millstone Hill and the Jicamarca data on 27 June to 1 July and 20–22 September 2006 are used in this study. It should be noted that COSMIC measurements with tangent points at the F_2 peak height within 6° latitude and 6° longitude of the ISR at Millstone Hill, and within 3° latitude and 9° longitude of the ISR at Jicamarca were selected for the profile comparison. The ISR median profiles within one hour time bin of the occultation are also required. Six typical electron density profiles at Millstone Hill and two profiles at Jicamarca are selected in the following comparisons.

[12] In Figure 3 the COSMIC electron density profiles are compared with those measured by the Millstone Hill ISR. Over Millstone Hill, these experiments use an interleaved alternating code (AC) and single pulse (SP) to make zenith measurements. The SP measurements with 480 μs pulse

JRO

(a) RO (11.7S, 84.76W)

DAY: 181

UTh: 06:35

(b) RO (9.79S, 81.67W)

DAY: 264

UTh: 00:58

—— COSMIC
●— ISR

Electron density (10^5 cm^{-3})

Figure 4. (a, b) Comparison of the COSMIC electron density profiles (solid lines) and the corresponding ISR profiles (circles) at Jicamarca (11.9°S, 76.0°W). Error bars are the standard deviations for the ISR data within a 1-hour time bin. Note that in Figure 4b the ISR data below 280 km are not shown because of spread F. The latitude and longitude of the RO electron density profile at the F_2 peak height are shown at the top of each panel.

length provide data spacing of 18 km while the AC measurements provide data spacing of 4.5 km. Note that the fundamental range resolution of 480 μs pulse length is 71.5 km, while data with 18 km resolution result from oversampling. The SP data are well suited for our comparisons above the peak height, because these are the heights where the radar range smearing effect can be ignored for SP measurements. The AC data carry nearly unbiased electron density information, so we use AC data below 400 km where the signal-to-noise ratio is large enough. Error bars (standard deviations) are also shown for the ISR data within a one hour time bin. It can be seen that there is good agreement between the COSMIC data and the ISR electron density profiles. The COSMIC retrieved electron density profiles are within the error bars of radar observations at all heights, except that the peak electron density in the

COSMIC data is larger than that of the ISR in Figure 3c (the difference is about 15%, which can probably be explained by the difference of location between the two measurements). The COSMIC and ISR data in this profile track each other well at other heights. The height of the F_2 peak also shows good agreement between the COSMIC and ISR data in these comparisons. In most cases the shapes of the ISR profiles are also captured by the COSMIC data.

[13] Figure 4 shows the comparison between the COSMIC retrieved electron density profiles and the corresponding ISR ones at Jicamarca. It can be seen that the RO retrieved F_2 peak height (h_mF_2) is in good agreement with Jicamarca ISR data, and the topside profile shape of both data sets also matches well. Compared with the ISR observations, the retrieved F_2 peak density (N_mF_2) is a little smaller in Figure 4a and larger in Figure 4b. However, in both cases presented in Figure 4, the RO tangential points were about 3 degrees in latitude or 6–9 degrees in longitude away from the ISR site, which is a significant separation at the magnetic equator. It is also worth mentioning here that it is very difficult to find a RO event that happens near an ISR site. Generally, however, the COSMIC data and electron densities from the two radars are in agreement, although their agreement is better at Millstone Hill than that at Jicamarca. This is probably due to the larger horizontal gradients at Jicamarca, which is ignored in the retrieval of the electron density profiles (see section 2).

[14] We also compared the retrieved peak electron density from the COSMIC measurements with those measured by 31 globally distributed ionosondes to perform a more extended validation. Ionosonde data were obtained from the National Geophysical Data Center (NGDC-NOAA) SPIDR database (http://spidr.ngdc.noaa.gov/spidr/). There are 276 coincident measurements made over one month (July 2006) for observations that had latitude/longitude differences between the COSMIC occultation and the ionosondes that were less than 2°. There is a strong correlation between the COSMIC N_mF_2 and those from ionosondes (Figure 5). The correlation coefficient was 0.85.

3.2. Comparison With IRI and TIEGCM Results

[15] We compared global maps of N_mF_2 and h_mF_2 obtained from COSMIC data in the northern summer (days 152–243, 2006) with similar maps from the IRI model and the TIEGCM (Figures 6 and 7). The latitudes and longitudes at the F_2 peak of the COSMIC RO electron density profiles have been used as inputs to the IRI model which was run using the appropriate geophysical conditions for each COSMIC orbit. The same grouping process was used to determine the global map of the F_2 peak values from the IRI model. The three-dimensional, time-dependent, first-principles model of the thermosphere and ionosphere, the NCAR-TIEGCM, was run for a characteristic day that was appropriate for this interval using the following inputs: day = 170, hemispheric power = 16 GW, cross-polar-cap potential = 45 kV and $F_{10.7} = 80 \times 10^{-22}$ W m^{-2} Hz^{-1}.

[16] Figure 6 is a set of contour plots of the peak density N_mF_2 as functions of geographic latitude and longitude from COSMIC measurements, IRI and TIEGCM results. In general, there is a good agreement between the COSMIC data and the IRI and TIEGCM model results. However, there are also some differences. There is an asymmetry in
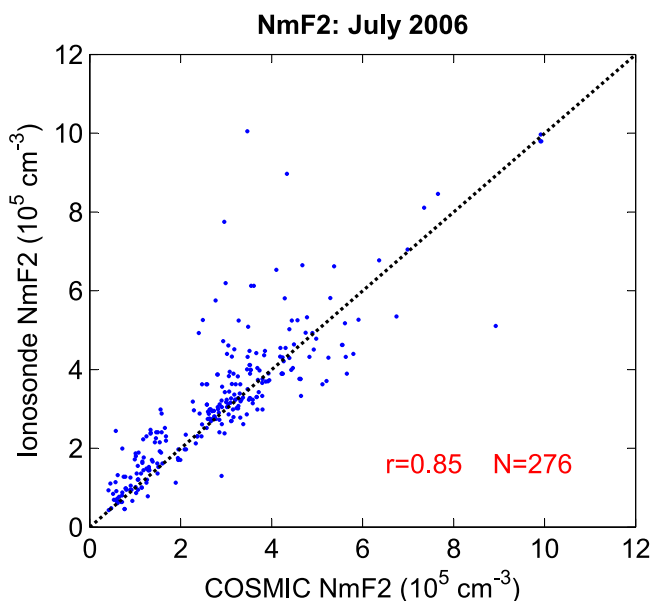
Figure 5. Correlation between the COSMIC N_mF_2 and those from ionosondes for the days $182-212$ (July), 2006. The number of data points N and the correlation coefficient r are also shown.

the equatorial ionospheric anomaly at the F_2 peak in the COSMIC data. For instance, we can see that COSMIC N_mF_2 is relatively lower at longitudes between $-60°$ and $60°$ at the northern crest than at the southern crest, whereas it is higher at longitudes between $-100°$ and $-60°$ at the northern crest than at the southern crest. The equatorial anomalies in the IRI results are basically symmetrical about the magnetic equator, although there are only small variations with the longitude. The IRI model overestimates the peak density in the crest region by up to $10-20\%$, which is consistent with the conclusion by *Jee et al.* [2005] that the IRI model tends to overestimate daytime TEC at low solar activity. The TIEGCM model can reproduce the asymmetry between the northern and southern equatorial anomalies and also produces a similar longitude variation like that seen in the COSMIC data, although its peak electron densities are about 10% lower than the peak electron densities retrieved from the COSMIC RO data in the equatorial regions. It also produces a discrete winter anomaly in the middle latitudes of the Southern Hemisphere. Both the COSMIC data and the IRI model indicate that higher electron densities occur in a similar middle latitude region, but the region in which these higher electron densities occur is not separate from the equatorial anomalies as it is in the TIEGCM results.

[17] The F_2 peak height (h_mF_2) maps of COSMIC measurements and IRI and TIEGCM results are given in Figure 7. The agreement appears to be good, but the scale tends to obscure any differences that do occur. A scatterplot (not given here) showed that the correlation between COSMIC h_mF_2 and IRI results in the Southern Hemisphere was poor, as h_mF_2 varied considerably over this hemisphere in the COSMIC data, but did not vary much in the IRI results. In the tropics, h_mF_2 in the Northern Hemisphere (summer) is much higher than it is in the Southern Hemisphere (winter).

This is probably associated with the thermospheric circulation which flows from the summer to the winter hemisphere. This issue will be discussed in detail in section 4.

4. Discussion

[18] The COSMIC retrieved electron density profiles are in agreement with those observed by ISRs in this limited set of overhead passes. This has significant implications for future ionospheric studies and space weather applications. Assimilated ground TEC observations may provide global electron density distributions [e.g., *Pi et al.*, 2003; *Schunk et al.*, 2004]; however, they cannot unambiguously determine F_2 peak electron densities, height and topside profiles. Tomographic inversions also can obtain the ionospheric electron density profiles, but they are limited to chains of stations in specific parts of the globe, for example, in the East Asian sector [see *Andreeva et al.*, 2000; *Yeh et al.*, 2001; *Tsai et al.*, 2002]. The COSMIC data provide vertical electron density profiles globally that are currently available only at a handful ISR sites, limited ionosonde locations, and along a few LEO satellite tracks other than those of COSMIC (e.g., CHAMP [*Jakowski et al.*, 2002]). The characteristics of ionospheric vertical profiles and their variations with changing geophysical conditions are of fundamental importance in understanding the thermospheric and ionospheric physics and for space weather applications.

[19] Initial COSMIC data show that there is a southern-northern asymmetry in the equatorial anomaly in the months of June, July, and August. As seen from Figures 6a and 7a, the following features can be found: (1) F_2 peak electron densities are larger at the winter (southern) crest than they are at the summer (northern) crest, and (2) the F_2 peak height in the winter (southern) hemisphere is about 100 km lower than the equivalent peak in the summer (northern) hemisphere. These features are consistent with previous observations [e.g., *Lyon*, 1963; *Thomas*, 1968]. The TIEGCM can reproduce both features well, whereas the IRI model captured only the second feature. The IRI results show that the northern and southern crests have roughly the same peak electron densities, whereas the COSMIC data and the NCAR-TIEGCM captures the asymmetries that have previously been seen in other data [*Thomas*, 1968; *Walker*, 1981].

[20] The possible mechanism for the southern-northern asymmetry during solstice is the prevailing summer-to-winter neutral winds [e.g., *Bramley and Young*, 1968; *Roble et al.*, 1977; *Thuillier et al.*, 2002]. There are strong trans-equatorial neutral winds blowing from the summer to the winter hemisphere at altitudes near the F_2 peak seen in the TIEGCM simulations (not shown). This neutral wind circulation moves the F region ionization upward to higher altitudes along the geomagnetic field lines in the Northern Hemisphere, but it moves the F region ionization downward in the Southern Hemisphere, resulting in the asymmetric structure of h_mF_2 (Figure 7). The summer-winter thermospheric circulation will also tend to reduce the fountain effect at the summer crest whereas it will tend to enhance the build up of ionization at the winter crest. Namely, in the summer (northern) hemisphere, the southward neutral winds have a component along the magnetic field lines that is in the opposite direction to field-aligned diffusion, thus limit-
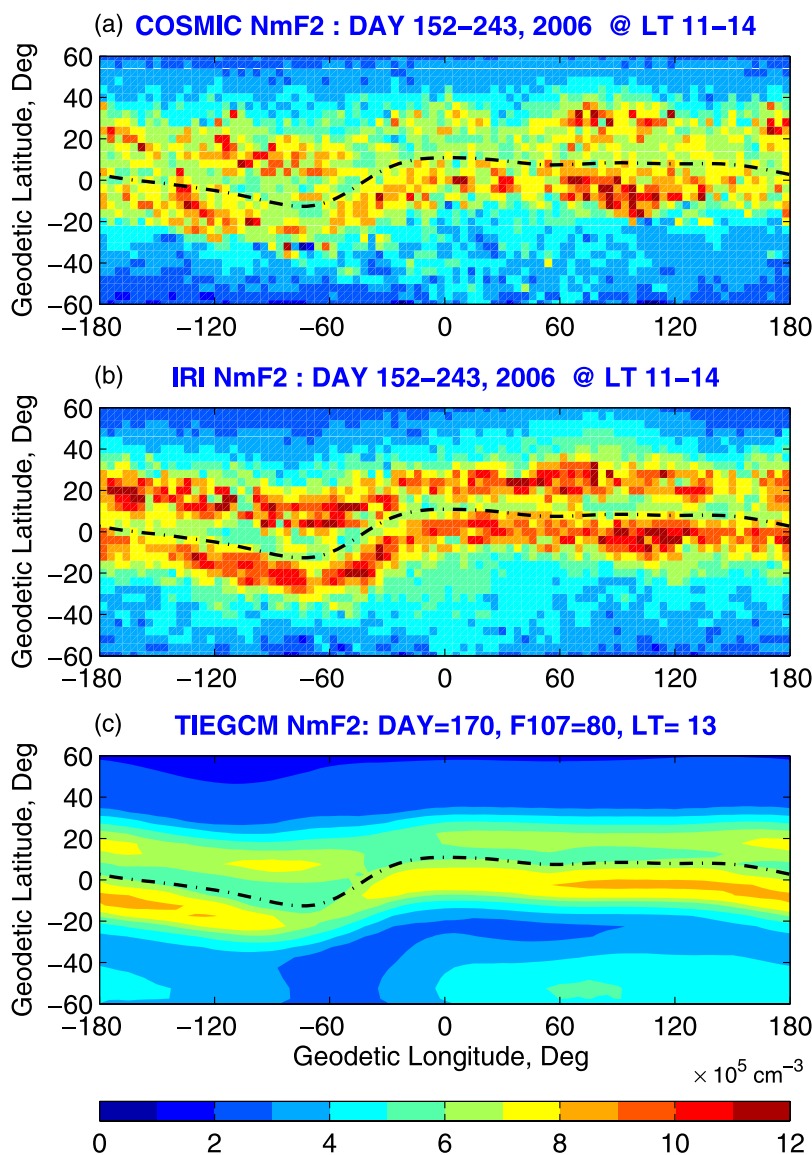
Figure 6. Global maps of daytime N_mF_2 derived from (a) COSMIC RO measurements and (b) the International Reference Ionosphere (IRI) model in the northern summer (days 152–243, 2006) and (c) calculated by the National Center for Atmospheric Research Thermosphere-Ionosphere-Electrodynamics General Circulation Model (NCAR-TIEGCM) in summer solstice (day 170). The dash-dotted lines indicate the location of the magnetic equator.

ing the development of the summer anomaly, whereas southward winds reinforce field-aligned diffusion in the winter (southern) hemisphere. The net result is to create the asymmetrical equatorial anomaly seen in the COSMIC data and TIEGCM results (Figure 6) where electron densities are smaller in the northern anomaly than they are in the southern one. A full diagnostic analysis of the ion continuity equation solved in the TIEGCM will be undertaken in the future to understand the physical processes that produce these features of the equatorial anomalies.

[21] There are significant longitudinal variations in COSMIC electron densities in the equatorial anomalies. For example, at the northern crest higher electron densities are seen at longitudes between $-130°$ and $-50°$ and between $60°$ and $120°$ (Figure 6). There are also longitudinal variations at the southern crest. These longitudinal varia-

tions are also seen in TIEGCM simulations. Several factors should contribute to the longitudinal variations in the equatorial anomaly. First, the effect of neutral winds in the equatorial region varies as a function of longitude because of the offset between the magnetic and geographic equators and the differences in magnetic declination [*Walker*, 1981; *Su et al.*, 1997]. Second, the equatorial electric fields and vertical drifts vary with longitude at a given local time. This is associated with zonal variations in the geomagnetic field and neutral winds [e.g., *Walker*, 1981; *Vichare and Richmond*, 2005, and references therein]. Finally, there are variations in electric fields due to the upward propagation of the tides and other waves from the lower atmosphere [*Walker*, 1981; *Immel et al.*, 2006; *England et al.*, 2006]. There are significant longitudinal variations in $E \times B$ vertical drift and F_2 region neural winds predicted by the
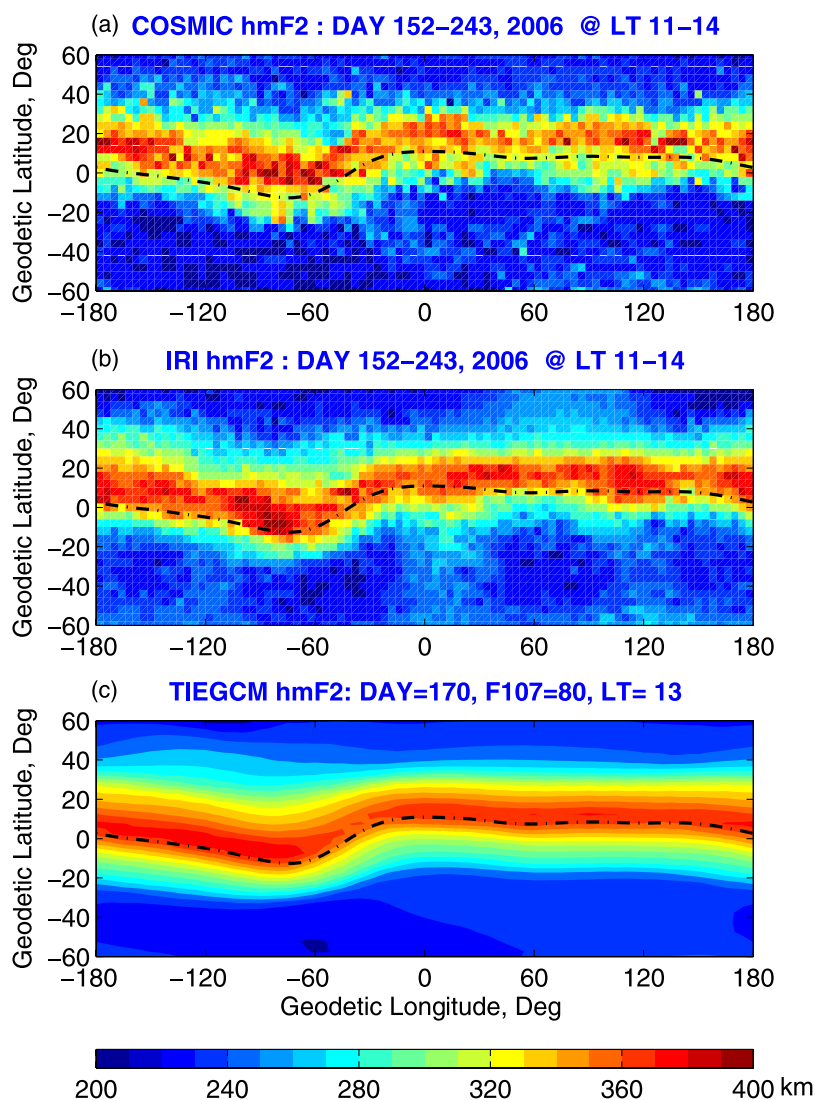
Figure 7. (a−c) Same as Figure 6 but for daytime h_mF_2.

TIEGCM (not shown). They may all contribute to the longitudinal variations in the equatorial anomaly seen in the COSMIC data and TIEGCM results (Figure 6). Further investigation is needed to explore the relative importance of different factors that lead to the longitudinal variations in the equatorial anomaly. We expect that when all six COSMIC satellites spread out to their final orbits, more local time and longitudinal coverage will be available to investigate these and other global ionospheric structures.

5. Conclusions

[22] We have compared electron density profiles retrieved from COSMIC RO measurements with those observed by ISR at Millstone Hill and Jicamarca for a limited number of overhead passes. These preliminary comparisons show that there is agreement between COSMIC retrieved density profiles and those observed by two ISRs (Millstone Hill and Jicamarca). Comparisons have also been made between COSMIC retrieved N_mF_2 values and those measured by global distributed ionosondes, and agreement is also obtained in this case. This indicates that electron density

profiles retrieved from COSMIC RO measurements are reliable and can be used for ionospheric physics studies. More extensive validation will be carried out as more data are collected by the COSMIC satellites.

[23] The comparison between the COSMIC data and the IRI model is also reasonably good, but some features such as the asymmetry of the equatorial anomaly in summer are not well represented by the IRI model. The IRI model also tends to overestimate N_mF_2 at the crests of the equatorial anomalies. The TIEGCM model can describe the equatorial anomaly structure obtained from the COSMIC measurements qualitatively, but there are some quantitative differences. The TIEGCM simulations also suggest that thermospheric neutral wind circulation from the summer hemisphere to the winter hemisphere may play an important role in the generation of the southern-northern asymmetry in the equatorial anomaly.

[24] In conclusion, the COSMIC derived ionospheric data appear to be consistent with other measurements and with model simulations in this preliminary validation study. We expect that COSMIC RO data measured when the satellites reach their final configuration will make significant contri-

butions to ionospheric studies, including the improvement of the global thermosphere/ionosphere models (both empirical and theoretical models) and space weather forecast.

Appendix A

[25] Under the assumption that the electron density varies linearly in between levels, the integrals in equation (4) can be solved analytically. After some effort we arrive at

$$
\tilde{T}(p_i) = \frac{p_{i+1}}{\Delta p_i} \left[\sqrt{p_{i+1}^2 - p_i^2} - \frac{p_i^2}{p_{i+1}} \ln\left(\frac{p_{i+1} + \sqrt{p_{i+1}^2 - p_i^2}}{p_i} \right) \right] N(p_i)
$$

$$
+ \sum_{k=1}^{m-1} \left\{ \frac{p_{i+k+1}}{\Delta p_{i+k}} \left[\sqrt{p_{i+k+1}^2 - p_i^2} - \sqrt{p_{i+k}^2 - p_i^2} \right. \right.
$$

$$
\left. - \frac{p_i^2}{p_{i+k+1}} \ln\left(\frac{p_{i+k+1} + \sqrt{p_{i+k+1}^2 - p_i^2}}{p_{i+k} + \sqrt{p_{i+k}^2 - p_i^2}} \right) \right]
$$

$$
- \frac{p_{i+k-1}}{\Delta p_{i+k-1}} \left[\sqrt{p_{i+k}^2 - p_i^2} - \sqrt{p_{i+k-1}^2 - p_i^2} \right.
$$

$$
\left. \left. - \frac{p_i^2}{p_{i+k-1}} \ln\left(\frac{p_{i+k} + \sqrt{p_{i+k}^2 - p_i^2}}{p_{i+k-1} + \sqrt{p_{i+k-1}^2 - p_i^2}} \right) \right] \right\} N(p_{i+k})
$$

$$
- \frac{p_{i+m-1}}{\Delta p_{i+m-1}} \left[\left(2 - \frac{p_{i+m}}{p_{i+m-1}} \right) \sqrt{p_{i+m}^2 - p_i^2} - \sqrt{p_{i+m-1}^2 - p_i^2} \right.
$$

$$
\left. - \frac{p_i^2}{p_{i+m-1}} \ln\left(\frac{p_{i+m} + \sqrt{p_{i+m}^2 - p_i^2}}{p_{i+m-1} + \sqrt{p_{i+m-1}^2 - p_i^2}} \right) \right] N(p_{i+m}), \quad (A1)
$$

where $\Delta p_i = p_{i+1} - p_i$. This form is not very convenient for numerical applications, because significant precision may be lost when subtracting almost identical, large terms. A form that better preserves numerical precision is obtained by introducing $\varepsilon_k = (p_{i+k} - p_i)/p_i$ for a given i. We can then write

$$
\tilde{T}(p_i) = p_i \left(c_{i,0} N(p_i) + \sum_{k=1}^{m-1} c_{i,k} N(p_{i+k}) + c_{i,m} N(p_{i+m}) \right), \quad (A2)
$$

with

$$
c_{i,0} = \varepsilon_1^{-1} \left[(1 + \varepsilon_1)\sqrt{\varepsilon_1(2 + \varepsilon_1)} - \ln\left(1 + \varepsilon_1 + \sqrt{\varepsilon_1(2 + \varepsilon_1)}\right) \right],
$$
(A3a)

$$
c_{i,k} = (\varepsilon_{k+1} - \varepsilon_k)^{-1} \left[(1 + \varepsilon_{k+1})\left(\sqrt{\varepsilon_{k+1}(2 + \varepsilon_{k+1})} \right. \right.
$$

$$
\left. - \sqrt{\varepsilon_k(2 + \varepsilon_k)} \right) - \ln\left(\frac{1 + \varepsilon_{k+1} + \sqrt{\varepsilon_{k+1}(2 + \varepsilon_{k+1})}}{1 + \varepsilon_k + \sqrt{\varepsilon_k(2 + \varepsilon_k)}} \right) \right]
$$

$$
- (\varepsilon_k - \varepsilon_{k-1})^{-1} \left[(1 + \varepsilon_{k-1})\left(\sqrt{\varepsilon_k(2 + \varepsilon_k)} \right. \right.
$$

$$
\left. - \sqrt{\varepsilon_{k-1}(2 + \varepsilon_{k-1})} \right) - \ln\left(\frac{1 + \varepsilon_k + \sqrt{\varepsilon_k(2 + \varepsilon_k)}}{1 + \varepsilon_{k-1} + \sqrt{\varepsilon_{k-1}(2 + \varepsilon_{k-1})}} \right) \right],
$$
(A3b)

$$
c_{i,m} = - (\varepsilon_m - \varepsilon_{m-1})^{-1} \left[(1 - \varepsilon_m + 2\varepsilon_{m-1})\sqrt{\varepsilon_m(2 + \varepsilon_m)} \right.
$$

$$
- (1 + \varepsilon_{m-1})\sqrt{\varepsilon_{m-1}(2 + \varepsilon_{m-1})}
$$

$$
\left. - \ln\left(\frac{1 + \varepsilon_m + \sqrt{\varepsilon_m(2 + \varepsilon_m)}}{1 + \varepsilon_{m-1} + \sqrt{\varepsilon_{m-1}(2 + \varepsilon_{m-1})}} \right) \right].
$$
(A3c)

[27] Zuyin Pu thanks Bodo W. Reinisch and another reviewer for their assistance in evaluating this paper.

References

Andreeva, E. S., S. J. Franke, K. C. Yeh, and V. E. Kunitsyn (2000), Some features of the equatorial anomaly revealed by ionospheric tomography, *Geophys. Res. Lett.*, *27*(16), 2465–2468.

Bilitza, D. (2001), International reference ionosphere 2000, *Radio Sci.*, *36*, 261–275.

Bramley, E. N., and M. Young (1968), Winds and electromagnetic drifts in the equatorial F2 region, *J. Atmos. Terr. Phys.*, *30*, 99–111.

England, S. L., T. J. Immel, E. Sagawa, S. B. Henderson, M. E. Hagan, S. B. Mende, H. U. Frey, C. M. Swenson, and L. J. Paxton (2006), Effect of atmospheric tides on the morphology of the quiet time, postsunset equatorial ionospheric anomaly, *J. Geophys. Res.*, *111*, A10S19, doi:10.1029/2006JA011795.

Garcia-Fernandez, M., M. Hernandez-Pajares, M. Juan, and J. Sanz (2003), Improvement of ionospheric electron density estimation with GPSMET occultations using Abel inversion and VTEC information, *J. Geophys. Res.*, *108*(A9), 1338, doi:10.1029/2003JA009952.

Hajj, G. A., and L. J. Romans (1998), Ionospheric electron density profiles obtained with the Global Positioning System: Results from the GPS/MET experiment, *Radio Sci.*, *33*, 175–190.

Hernandez-Pajares, M., J. M. Juan, and J. Sanz (2000), Improving the Abel inversion by adding ground GPS data to LEO radio occultations in ionospheric sounding, *Geophys. Res. Lett.*, *27*, 2473–2476.

Immel, T. J., E. Sagawa, S. L. England, S. B. Henderson, M. E. Hagan, S. B. Mende, H. U. Frey, C. M. Swenson, and L. J. Paxton (2006), The control of equatorial ionospheric morphology by atmospheric tides, *Geophys. Res. Lett.*, *33*, L15108, doi:10.1029/2006GL026161.

Jakowski, N., A. Wehrenpfennig, S. Heise, C. Reigber, H. Lühr, L. Grunwaldt, and T. K. Meehan (2002), GPS radio occultation measurements of the ionosphere from CHAMP: Early results, *Geophys. Res. Lett.*, *29*(10), 1457, doi:10.1029/2001GL014364.

Jee, G., R. W. Schunk, and L. Scherliess (2005), Comparison of IRI-2001 with TOPEX TEC measurements, *J. Atmos. Sol. Terr. Phys.*, *67*, 365–380.

Lei, J., L. Liu, W. Wan, S.-R. Zhang, and J. M. Holt (2004), A statistical study of ionospheric profile parameters derived from Millstone Hill incoherent scatter radar measurements, *Geophys. Res. Lett.*, *31*, L14804, doi:10.1029/2004GL020578.

Lei, J., L. Liu, W. Wan, and S.-R. Zhang (2005), Variations of electron density based on long-term incoherent scatter radar and ionosonde measurements over Millstone Hill, *Radio Sci.*, *40*, RS2008, doi:10.1029/2004RS003106.

Lyon, A. J. (1963), The geomagnetic anomaly, in *Proceedings of the International Conference on the Ionosphere*, edited by A. C. Strickland, pp. 88–93, Inst. of Phys. and the Phys. Soc., London.

Pi, X., C. Wang, G. A. Hajj, G. Rosen, B. D. Wilson, and G. J. Bailey (2003), Estimation of E × B drift using a global assimilative ionospheric model: An observation system simulation experiment, *J. Geophys. Res.*, *108*(A2), 1075, doi:10.1029/2001JA009235.

Richmond, A. D., E. C. Ridley, and R. G. Roble (1992), A thermosphere/ionosphere general circulation model with coupled electrodynamics, *Geophys. Res. Lett.*, *19*, 601–604.

Roble, R. G., R. E. Dickinson, and E. C. Ridley (1977), Seasonal and solar cycle variations of the zonal mean circulation in the thermosphere, *J. Geophys. Res.*, *82*, 5493–5504.

Rocken, C., Y.-H. Kuo, W. Schreiner, D. Hunt, S. Sokolovskiy, and C. McCormick (2000), COSMIC system description, *Terr. Atmos. Ocean Sci.*, *11*, 21–52.

Schreiner, W. S., S. V. Sokolovsky, C. Rocken, and D. C. Hunt (1999), Analysis and validation of GPS/MET radio occultation data in the ionosphere, *Radio Sci.*, *34*, 949–966.

Schreiner, W., C. Rocken, S. Sokolovsky, S. Syndergaard, and D. Hunt (2007), Estimates of the precision of GPS radio occultations from the COSMIC/FORMOSAT-3 mission, *Geophys. Res. Lett.*, *34*, L04808, doi:10.1029/2006GL027557.

Schunk, R. W., et al. (2004), Global Assimilation of Ionospheric Measurements (GAIM), *Radio Sci.*, *39*, RS1S02, doi:10.1029/2002RS002794.

Su, Y. Z., G. J. Bailey, K. I. Oyama, and N. Balan (1997), A modelling study of the longitudinal variations in the north-south asymmetries of the ionospheric equatorial anomaly, *J. Atmos. Terr. Phys.*, *59*, 1299–1310.

Syndergaard, S. (2002), A new algorithm for retrieving GPS radio occultation total electron content, *Geophys. Res. Lett.*, *29*(16), 1808, doi:10.1029/2001GL014478.

Syndergaard, S., W. S. Schreiner, C. Rocken, D. C. Hunt, and K. F. Dymond (2006), Preparing for COSMIC: Inversion and analysis of ionospheric data products, in *Atmosphere and Climate: Studies by Occultation Methods*, edited by U. Foelsche, G. Kirchengast, and A. K. Steiner, pp. 137–146, Springer-Verlag, Berlin.

Thomas, L. (1968), The F2-region equatorial anomaly during solstice periods at sunspot minimum, *J. Atmos. Terr. Phys.*, *30*, 1631–1640.

Thuillier, G., R. H. Wiens, G. G. Shepherd, and R. G. Roble (2002), Photochemistry and dynamics in the thermospheric intertropical arcs measured by the WIND Imaging Interferometer on board UARS: A comparison with TIE-GCM simulations, *J. Atmos. Sol. Terr. Phys.*, *64*, 405–415.

Tsai, L.-C., and W.-H. Tsai (2004), Improvement of GPS/MET ionospheric profiling and validation using Chung-Li ionosonde measurements and the IRI model, *Terr. Atmos. Oceanic Sci.*, *15*, 589–607.

Tsai, L.-C., C. H. Liu, W. H. Tsai, and C. T. Liu (2002), Tomographic imaging of the ionosphere using the GPS/MET and NNSS data, *J. Atmos. Sol. Terr. Phys.*, *64*, 2003–2011.

Vichare, G., and A. D. Richmond (2005), Simulation study of the longitudinal variation of evening vertical ionospheric drifts at the magnetic equator during equinox, *J. Geophys. Res.*, *110*, A05304, doi:10.1029/2004JA010720.

Walker, G. O. (1981), Longitudinal structure of the *F* region equatorial anomaly: A review, *J. Atmos. Terr. Phys.*, *43*, 763–774.

Yeh, K. C., S. J. Franke, E. S. Andreeva, and V. E. Kunitsyn (2001), An investigation of motions of the equatorial anomaly crest, *Geophys. Res. Lett.*, *28*(24), 4517–4520.

————————

A. G. Burns, J. Lei, R. G. Roble, S. C. Solomon, W. Wang, Q. Wu, and Z. Zeng, High Altitude Observatory, National Center for Atmospheric Research, 3080 Center Green, Boulder, CO 80307-3000, USA. (aburns@ucar.edu; leijh@ucar.edu; stans@ucar.edu; wbwang@ucar.edu)

J. M. Holt and S.-R. Zhang, Haystack Observatory, Massachusetts Institute of Technology, Route 40, Westford, MA 01886, USA.

D. L. Hysell and F. S. Rodrigues, Department of Earth and Atmospheric Science, Cornell University, 2108 Snee Hall, Ithaca, NY 14853, USA.

Y.-H. Kuo and S. Syndergaard, University Corporation for Atmospheric Research, Boulder, CO 80307-3000, USA. (ssy@ucar.edu)

C. H. Lin, National Space Organization, Hsinchu 30078, Taiwan.